Highly Efficient Laser Scribed Graphene Electrodes for On-Chip Electrochemical Sensing Applications

Pranati Nayak, Narendra Kurra, Chuan Xia, and Husam N. Alshareef*

This study reports the fabrication of flexible electrochemical sensors using a direct-write laser scribing process that transforms commercial polyimide sheet into graphitic carbon with self-standing porous 3D morphology, and abundant edge planes. The heterogeneous electron transfer rate (k^0) of the laser scribed graphene (LSG) electrodes for both inner-sphere and outer-sphere redox mediators, ferrocyanide ([Fe(CN)$_6$]$^{4-}$) and hexaammineruthenium ([Ru(NH$_3$)$_6$]$^{3+}$) are estimated to be 0.1150 and 0.0868 cm s^{-1}, respectively. These values are significantly higher than those for similar carbon based materials, which this study ascribes to the binder free 3D porous network of LSG with enriched edge plane sites. Further, k^0 is enhanced up to 0.2823 and 0.2312 cm s^{-1} for inner and outer-sphere redox mediators by selective anchoring of Pt nanoparticles over LSG. The LSG electrodes exhibit significantly improved electrocatalytic activity toward oxidation of ascorbic acid (AA), dopamine (DA), and uric acid (UA). Consequently, the detection of these biomarkers is achieved with high sensitivity of 237.76 and 250.69 µA mм$^{-1}$ cm^{-2} (AA), 2259.9 and 6995.6 µA mм$^{-1}$ cm^{-2} (DA) and 5405 and 8289 µA mм$^{-1}$ cm^{-2} (UA) for LSG and Pt/LSG electrodes, respectively, in a wide concentration range. These results outperform previously reported 2D/3D graphene based electrodes.

1. Introduction

Carbon based materials stretching from graphite to graphene with various surface morphologies and functionalities have been overwhelmingly used for electrochemical sensing applications.[1] Structure, morphology, porosity, and surface functionality of the carbon electrode have a direct impact on electron transfer rate and hence its analytical performance. For example, it was demonstrated that electron transfer kinetics are tremendously enhanced at graphene edge sites due to rich in corrugations and defect densities, whereas it is slower and less pronounced at the basal plane.[2] Hence, in order to achieve an optimum electrochemical performance, while in-plane functionality of material is more imperative, the use of graphene for electrochemical transduction, sensing, or as a host of catalyst and biological molecules ideally require a 3D architecture with retained "2D" properties of the material.[3] Numerous reports have claimed that an enhanced electrochemical response was obtained when graphene is patterned into porous 3D network structure, due to its large specific surface area and a highly conductive pathways stimulating adequate efficiency in charge transfer and mass transport.[3b,4] Though these layouts offer excellent functionality, the devices fabricated from these materials are commonly realized by standard microfabrication involving spin/spray-coating or sometimes screen printing techniques that are either expensive or require additional binders or additives, which can be detrimental for electrochemical sensing applications.[3a,5] In spite of this, the complex solution processing of graphene derived materials leads aggregation and re-stacking between individual graphene sheets as a result of the strong sheet-to-sheet van der Waals interactions, greatly compromising the intrinsic high specific surface area and hence lessening the electrochemical activity.[5b,6] These issues limit their integration with functional on-chip device applications. Hence, it is highly challenging to fabricate the graphitic carbon materials with desired surface functionality, having 3D architecture enriched with edge planes, while avoiding complex solution processing and additive/binder-free approach.

Computer aided laser scribing technique to produce reduced graphene oxide pattern from solution processed graphite oxide (GO) opened up a new direction in direct on-chip fabrication of micropower units by Kaner group.[7] However, this technique still requires multi-step chemical processing before patterning. Here, we adopt a direct writing process to fabricate patterns of graphitic carbon on commercial flexible polyimide (PI) surface employing a laser scribing approach, a process that has been reported by the Tour group for fabricating 3D microsupercapacitor.[8] Interestingly, the proposed process offers a binder-free, porous, conductive carbon with 3D interconnected network, rich in defects and edge plane sites, but still functional enough to be wetted by the aqueous electrolytes, making it a potential electrode material for electrochemical sensing applications. Also, this self-supporting architecture offers large specific surface area, which can facilitate the electrolyte accessibility to the electrode surfaces and hence is favorable for electrochemical sensing. In addition, direct writing of the electrochemical sensors can enable integration of these sensors with other electronic and energy storage elements (e.g., microsupercapacitors, thin-film batteries, and printed electronics). The above

Dr. P. Nayak, Dr. N. Kurra, C. Xia, Prof. H. N. Alshareef
Materials Science and Engineering
King Abdullah University of Science
and Technology (KAUST)
Thuwal 23955-6900, Saudi Arabia
E-mail: husam.alshareef@kaust.edu.sa

characteristics make the 3D graphitic carbon electrode a promising platform for on-chip printed electrochemical sensing applications, which prompted us to explore its electrochemical behavior against various redox mediators and to use it as sensor. Further, the conducting nature of 3D graphitic structure allowed us in decorating metal nanoparticles by a simple electrodeposition process to improve the electron transfer behavior and sensitivity of the electrochemical sensor. Finally, we show that these proto-type co-planar electrochemical sensors can have superior heterogeneous electron transfer (HET) kinetics, while being selective and sensitive to biomarkers including ascorbic acid, dopamine and uric acid.

2. Results and Discussion

2.1. Characterization of LSG Based Electrodes

The fabrication scheme of 3D porous graphitic co-planar electrodes for electrochemical sensing of biomarkers is demonstrated in **Figure 1**. As shown in Figure 1a,b, direct laser scribing was used to fabricate LSG co-planar three-electrode patterns (labeled as working, WE; counter, CE, and reference electrode, RE) on a PI sheet (see the optical images of device in Figure S1 in the Supporting Information). Upon laser scribing, the orange colored PI surface gets transformed into black 3D carbonaceous material (as the thickness >10 μm), as depicted from the schematic illustration. The obtained carbon patterns have a typical thickness of around ≈33 μm (projected cross-sectional scanning electron microscopy (SEM) image in Figure 1b and Figure S2a in the Supporting Information). The active portion of the sensing area was isolated from the rest of the pattern by selective passivation using hydrophobic polydimethylsiloxane (PDMS) as shown in the Figure 1c (see the optical image shown in Figure S1b in the Supporting

Information). Previously, screen printing or ink-jet printing of activated carbon was employed in fabricating three-electrode architecture for printed electrochemical sensing applications. Since the electrode architecture in our study is similar to those of standard commercial electrodes, it is also fair to compare the intrinsic electrochemical performance of our 3D porous graphitic carbon obtained via laser scribing with other forms of carbon materials which we will show later in the manuscript. Electrodeposition of Pt nanoparticles (Pt NPs) over LSG was done in order to enhance the catalytic activity (Figure 1d). The loading of Pt NPs in the composites (≈28 wt%) was easily controlled by adjusting the deposition time or cycles, and is here labeled as Pt/LSG.[9] The digital photograph in Figure 1e shows 6 × 9 array of co-planar three-electrode patterns over a PI sheet, clearly showing a scalable fabrication process.

The morphology of as-obtained LSG was characterized using SEM. **Figure 2**a–c illustrate the top-view SEM and transmission electron microscopy (TEM) images of the as-prepared LSG. The morphology is seen to be porous with 3D perspective, abundant of edge-plane sites as shown in the SEM micrographs (see Figure S2 in the Supporting Information). It was reported that a focused laser beam could produce high local temperatures (>2500 °C), which helps in carbonization and graphitization of polymer surfaces. As this laser scribing was performed in air, the local availability of oxygen, and moisture during the graphitization process could burn-off some amount of carbon, resulting in the porous nature. The available edge-plane sites on the surface of the LSG pattern are expected to enhance electron transfer behavior, whereas the intact 3D morphology offers high accessible electrochemical surface area. The homogeneous deposition of Pt NPs on LSG is confirmed by the SEM and TEM images shown in Figure 2d–f. The SEM elemental mapping and energy dispersive X-ray analysis (EDX) are shown in **Figure 3**a–c (EDX in insets of a and d) for LSG and Figure 3d–g for Pt/LSG, showing C, O and uniform anchoring of Pt NPs on Pt/LSG.
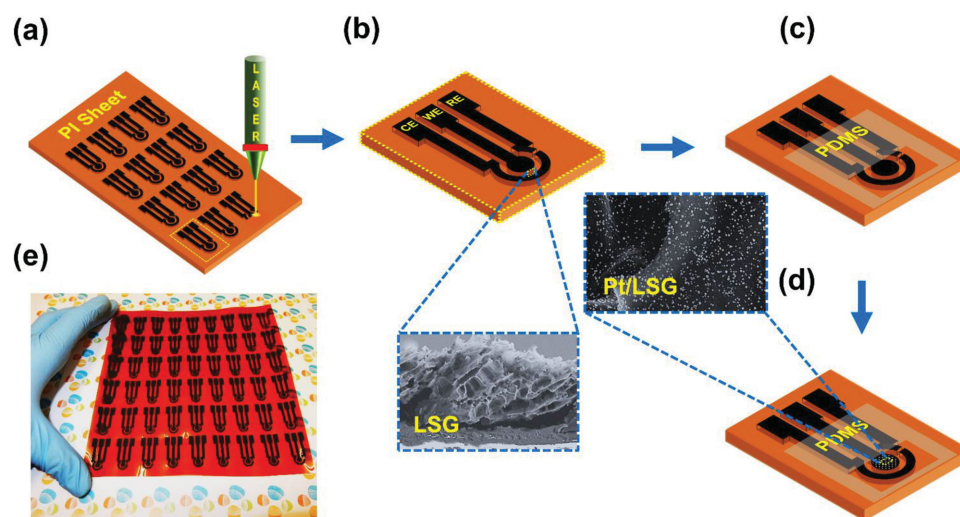
Figure 1. Schematic illustration of the fabrication of LSG and Pt/LSG electrode patterns on PI sheet. a) Fabrication of arrays of electrodes on PI sheet by laser scribing. b) 3D view of the LSG electrode pattern. The projection displays vertical cross-sectional SEM image of a laser-scribed PI sheet showing porous and protruded morphology of graphene. c) Selective passivation of electrode area by a PDMS. d) Electrodeposition of Pt NPs selectively on the working electrode area. The projection displays SEM image of homogeneously anchored Pt NPs over graphene sheets. e) Digital photograph of patterned electrode arrays on PI sheet.

www.MaterialsViews.com

ADVANCED
ELECTRONIC
MATERIALS
www.advelectronicmat.de

FULL PAPER
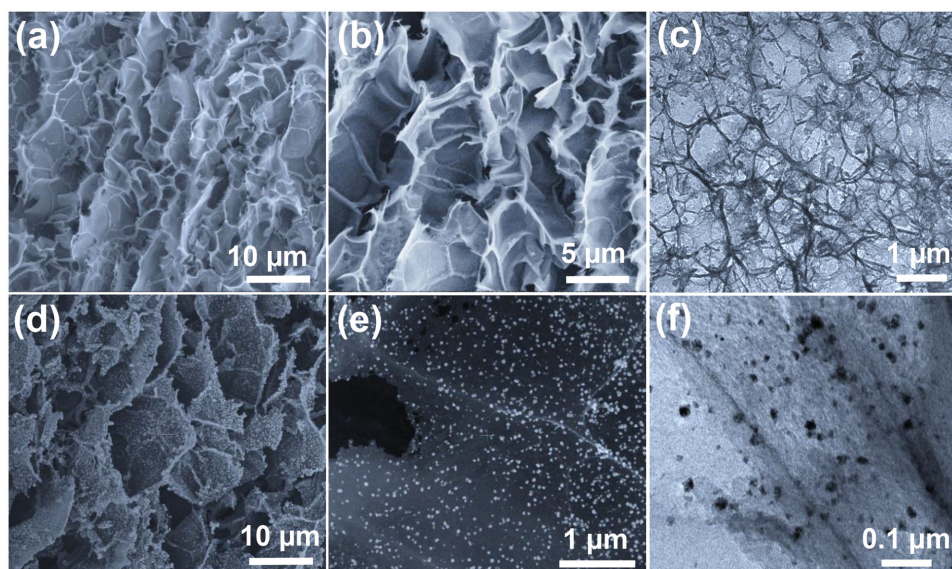
Figure 2. Morphology of 3D porous graphitic carbon. a,b) SEM images of LSG at different magnifications. c) TEM image of LSG. d,e) SEM images of Pt/LSG displaying anchored Pt NPs over LSG at different magnifications. f) TEM image of the Pt/LSG.

The structural characteristics of LSG and Pt/LSG electrodes were investigated by X-ray diffraction (XRD) and Raman spectroscopy. The XRD pattern confirms the graphitic structure of LSG as indicated by the presence of the typical C (002) peak at $2\theta = 26.42°$ with corresponding interlayer spacing of ≈0.34 nm (d_{002}) (Figure 3h).[10] Along with this, the broadening depicts

disorder in c-axis periodicity of 3D graphitic structure. For Pt/LSG, the XRD data shows major peaks between $2\theta = 35$ and 85° along with C (002) peak. These peaks can be indexed to simple cubic structure of Pt (JCPDS No-87-0646). The peak corresponding to C (100) graphitic crystal phase was also present. The X-ray photoelectron spectra (XPS) of LSG and Pt/LSG show
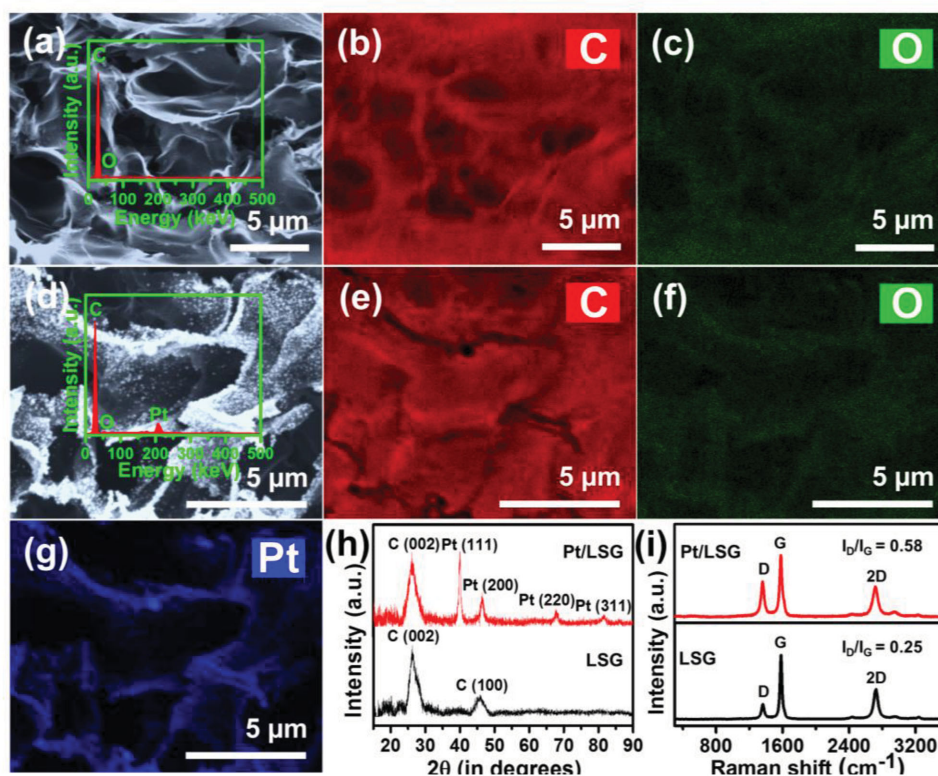
Figure 3. a) SEM image of LSG (insets shows EDX) and its corresponding elemental mapping images of b) C and c) O, d) SEM image of Pt/LSG (insets shows EDX) and its corresponding elemental mapping images of e) C, f) O, and g) Pt. h) XRD patterns and i) Raman spectra of the LSG and Pt/LSG.

the presence of sp^2-C peak and O peak (Figure S3 and Table S1, Supporting Information). The presence of peak corresponding to Pt in the survey spectrum of Pt/LSG again confirms successful electrodeposition of Pt NPs on LSG. Graphitization of the PI sheet upon laser scribing was probed through Raman. As shown in Figure 3i, three dominant peaks are observed: D band (induced by bent sp^2 carbon bonds by breaking translational symmetry, essentially defect sites/functional groups), G band (corresponds to the E_{2g} vibration mode of graphitic carbon), and 2D band.[11] The laser scribing process seems to trigger the depolymerization of polyimide, cause carbonization and subsequent graphitization, resulting in the formation of the graphitic domains. As this process is carried out under ambient conditions, availability of surplus amount of oxygen and water molecules in the surrounding environment under such high temperature conditions react with graphitic carbon releasing some of it in the form of CO and CO_2 gases. However, the non-uniform distribution of oxygen, water molecules and intense laser energy actually produces an intricate morphology of 3D porous graphitic carbon in this laser scribing process. The details of Raman spectra features are tabulated in Table S2 in the Supporting Information. The typical I_D/I_G ratio for LSG is found to be 0.25, while that for Pt/LSG is ≈0.58, which is probably due to the introduction of more defects with the attachment of metal nanoparticles. Besides, the full width at half maximum (FWHM) of G band and 2D band increases by 31.3% and 18.5%, respectively for Pt/LSG, which indicates interaction of Pt NPs with graphene.[12] Thus, the laser scribing process is able to graphitize the polyimide surface without aid of metal catalyst, which is an attractive feature of the process.

In order to study the accessibility of electrolyte to the electrode material, the wettability of the electrode material was evaluated by contact angles measurement (see Figure S4 and video in the Supporting Information). The LSG shows partially hydrophilic in nature, which could facilitate the diffusion of aqueous electrolyte.

2.2. Cyclic Voltammetry Measurements

To gain insight into intrinsic electrochemical activity of LSG, we first investigated the HET mechanism of the fabricated LSG based devices employing two different electrochemical redox mediators. Consequently, the intrinsic electrochemical behavior qualifies it for electrochemical sensing application. The macro/mesoporous structure of LSG could facilitate easy access to the electrolyte ions into the carbon active material, while the good electrical conductivity of the 3D porous graphitic network could be helpful for electrodeposition of metal nanoparticles that may improve the electron transfer and catalytic activity. Here, we employ 3D graphitic carbon as working and counter electrodes while external Ag/AgCl was employed as reference electrode. Initially, we have examined the usage of LSG as a reference electrode instead of conventional Ag/AgCl reference electrode (discussed in Figure S5 in the Supporting Information). Sometimes, it may be possible to use carbon as a quasi-reference electrode, but in order to probe the intrinsic electrochemical property of 3D graphitic carbon while eliminating the additional factors, such as external interference, we have chosen standard Ag/AgCl as reference throughout this study.

A series of cyclic voltammograms (CVs) were recorded for LSG and Pt/LSG electrodes using both inner-sphere ([Fe(CN)$_6$]$^{4-}$) and outer-sphere ([Ru(NH$_3$)$_6$]$^{3+}$) redox mediators each at a concentration of 5×10^{-3} M dissolved in 0.1 M KCl aqueous solution. The results were compared to edge plane pyrolytic graphite (EPPG) and basal plane pyrolytic graphite (BPPG) electrodes of same diameter as of our LSG working electrode, which is shown in **Figure 4**a,b. It is acclaimed that the electrochemistry of graphene-based materials resembles that of the EPPG electrode, which is rich in defects and oriented edges.[13] The CVs illustrate electron transfer between the LSG electrode and the redox mediator with the corresponding reduction and oxidation of the mediator species. It is observed from the voltammetry profiles that [Fe(CN)$_6$]$^{4-}$ shows a lower ΔE_p value for EPPG compared to BPPG electrodes indicating a faster HET rate since EPPG is rich in edge plane sites, which readily accelerate the electron transfer process. It is meaningful for [Fe(CN)$_6$]$^{4-}$ being an inner-sphere redox mediator with inherent sensitivity toward the density of electronic states (DOS) near the Fermi level of the carbon materials and more prominently to the surface microstructures.[14] The CV response of LSG exhibits a lesser ΔE_p value compared to EPPG and BPPG electrodes, with a large redox current density (J_p) indicating faster electron transfer mechanism and enhanced electrochemical active surface area (A). In comparison, lower ΔE_p and increase in J_p is observed for Pt/LSG, which indicates comparatively better HET, presumably due to catalytic activity of surface anchored Pt NPs. The electrochemical active surface area (A) for LSG and Pt/LSG electrodes were estimated based on the Randles–Sevcik equation, which assumes mass transport only by diffusion process[15]

$$I_p = 2.69 \times 10^5 \, A D^{1/2} n^{3/2} \vartheta^{1/2} C \tag{1}$$

where n is the number of electrons participating in the redox reaction, D is the diffusion coefficient of the molecule ($D = 6.70 \times 10^{-6}$ cm^2 s^{-1} for [Fe(CN)$_6$]$^{4-}$ and 8.43×10^{-6} cm^2 s^{-1} for [Ru(NH$_3$)$_6$]$^{3+}$), C is the concentration of the probe molecule in the solution (mol cm^{-3}), and ϑ is the scan rate (V s^{-1}).[16] The calculated average A value for the LSG WE is found to be ≈9.177 mm^2 while it is ≈10.383 mm^2 for the Pt/LSG WE. Thus, the addition of Pt nanoparticles increased the effective electrode surface area by roughly 13.14%, which is only slightly higher than that of LSG electrode. Figure 4b compares the CV profile in the presence of 5×10^{-3} M [Ru(NH$_3$)$_6$]$^{3+}$ with EPPG, BPPG, LSG, and Pt/LSG electrodes. Interestingly, EPPG and BPPG exhibit similar behavior directly evidencing [Ru(NH$_3$)$_6$]$^{3+}$ redox mediator following an outer-sphere redox mechanism, which is mainly influenced by the DOS and independent of the microstructure of the electrode material. Again the CV response for LSG and Pt/LSG exhibit lesser ΔE_p value with a large redox current density (J_p) compared to EPPG and BPPG electrodes, indicating faster electron transfer mechanism. The repeatability of the fabricated microelectrodes was studied by measuring CV for same electrolyte with five different electrodes (Figure 4c), which indicates reproducible redox current. Further confirmation has been achieved by taking different redox mediators for LSG based electrodes (see Figure S6 in the Supporting Information). Again, surface passivation/blocking of the electrode

www.MaterialsViews.com

**ADVANCED
ELECTRONIC
MATERIALS**
www.advelectronicmat.de

FULL PAPER
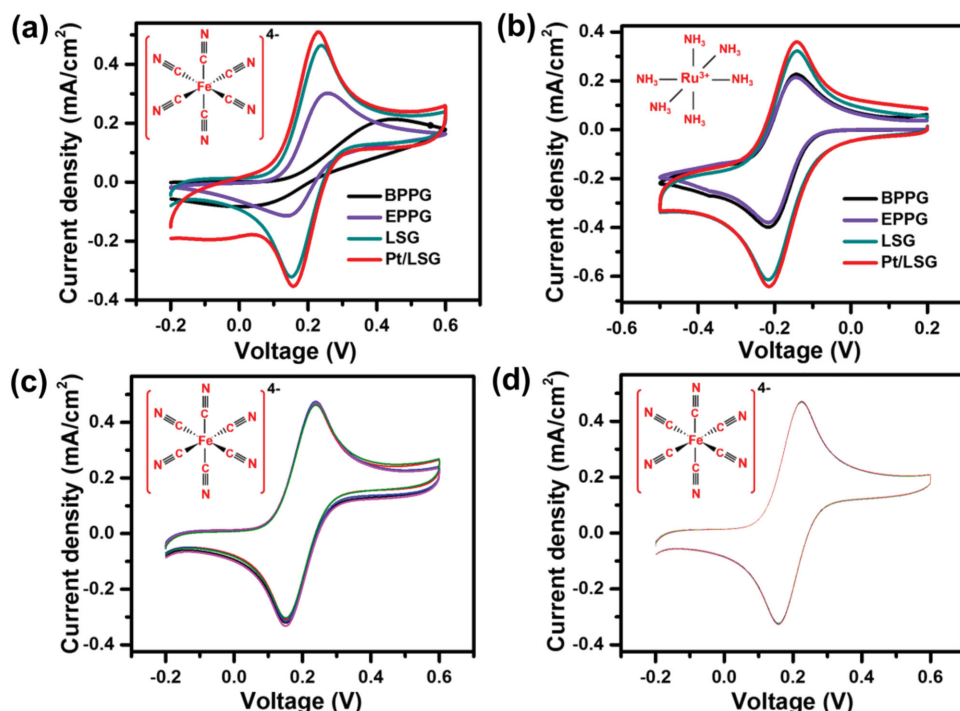
Figure 4. Cyclic voltammograms of LSG based electrodes. CVs for a) 5×10^{-3} M [Fe(CN)$_6$]$^{4-}$ and b) 5×10^{-3} M [Ru(NH$_3$)$_6$]$^{3+}$ on LSG and Pt/LSG compared with BPPG and EPPG at a scan rate 10 mV s^{-1}. c) CVs for 5×10^{-3} M [Fe(CN)$_6$]$^{4-}$ at 10 mV s^{-1} scan rate for five different LSG electrodes. d) Repeat CVs for 5×10^{-3} M [Fe(CN)$_6$]$^{4-}$ at 10 mV s^{-1} scan rate on LSG electrode. Each cycle was run at 5 min intervals; for a total of 20 cycles. All measurements were performed relative to external Ag/AgCl (3 M KCl) reference electrode and 0.1 M KCl solution was used as supporting electrolyte.

surface by repeated cycling of electrode material is an important aspect for its re-usability in sensor application. Therefore, we investigated both LSG and Pt/LSG electrodes by allowing the same electrode to be dipped in solution and recording the CVs at 5 min intervals for up to 20 cycles (Figure 4d). Interestingly, no significant change in ΔE_p value or deterioration in J_p was observed, which is unique behavior of the 3D graphitic carbon produced by this method unlike the previously reported literature on surface passivation by inner-sphere redox mediators being chemisorbed on the electrode surface, consequently affecting the exposed surface.[17] Optimal oxygen functionalities, that are sufficient enough for wettability of LSG, can be the plausible explanation for this positive feature, since [Fe(CN)$_6$]$^{4-}$ redox mediator is more sensitive to oxygen functionalities in carbon based materials.[18]

Figure 5 depicts the CVs recorded at different scan rates for both inner and outer-sphere redox mediators [[Fe(CN)$_6$]$^{4-}$ (a and b) and [Ru(NH$_3$)$_6$]$^{3+}$ (c and d)] at LSG and Pt/LSG electrodes, respectively. The reaction appears to be quasi-reversible in nature, resulting in monotonic increase of J_p with square root of scan rate ($\vartheta^{1/2}$), indicating a diffusion controlled voltammetry response for both redox mediators (upper inset of CVs). This allows the HET rate (k^0) to be determined, using the analysis developed by Nicholson[19]

$$\Psi = k^0 \left(\frac{D_O}{D_R} \right)^{\alpha/2} \sqrt{\frac{RT}{\pi n F D_O \vartheta}} \qquad (2)$$

where Ψ is the dimensionless kinetic parameter determined from ΔE_p, D_O / D_R are the diffusion coefficients of the

oxidized/reduced form of the electroactive species, α is the transfer coefficient, n is the number of electrons transferred in the electrochemical reaction, F is the Faraday constant ($F = 96\ 489$ C mol^{-1}), ϑ is the scan rate in V s^{-1}, R is the universal gas constant (8.314 J K^{-1} mol^{-1}) and T is the absolute temperature.

Assuming the D_O and D_R to be approximately equal and symmetrical redox kinetics ($\alpha \approx 0.5$) of the redox mediator, Equation (2) simplifies to

$$\Psi = k^0 \sqrt{\frac{RT}{\pi F D \vartheta}} \qquad (3)$$

or

$$\Psi = C k^0 \vartheta^{-1/2} \qquad (4)$$

For a one electron process, Ψ depends on ΔE_p and can be determined from the following equation

$$\Psi = \frac{(-0.6288 + 0.0021\ X)}{(1 - 0.017\ X)} \qquad (5)$$

where X is equal to the peak potential separation (ΔE_p) of the system multiplied by the number of electrons involved in the electrochemical reaction (n). Therefore using Equations (4) and (5), k^0 can be determined from the slope of Ψ versus $C\vartheta^{-1/2}$ plot as shown in lower insets of Figure 5. Each time the CV has been conducted and electrochemical parameters were determined for a set of five separate LSG and Pt/LSG electrodes (CVs for other

ADVANCED
ELECTRONIC
MATERIALS
www.advelectronicmat.de

Materials
Views
www.MaterialsViews.com
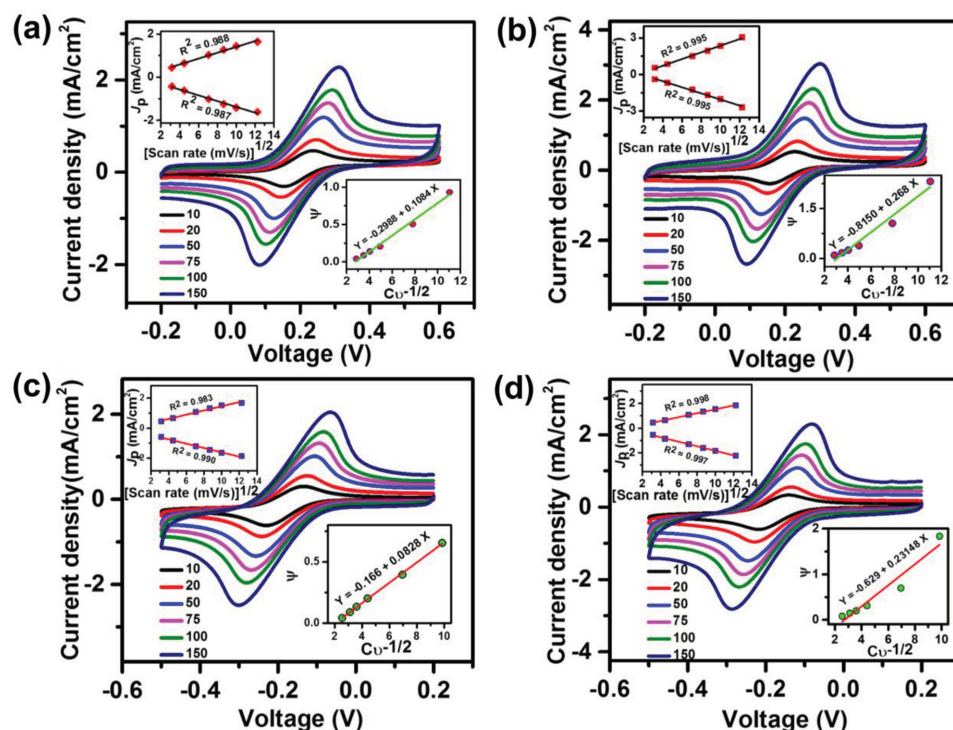
Figure 5. Cyclic voltammograms and allied kinetic analyses at LSG and Pt/LSG electrodes. CVs of a,b) 5×10^{-3} M $[Fe(CN)_6]^{4-}$ and c,d) 5×10^{-3} M $[Ru(NH_3)_6]^{3+}$ at different scan rates for LSG and Pt/LSG electrodes in 0.1 M KCl solution as supporting electrolyte. Insets (upper left) show plot of measured redox peak current density (J_p) versus square root of scan rate ($v^{1/2}$). Inset (lower right): plot of Nicholson's kinetic parameter Ψ versus C multiplied by reciprocal of the square root of the scan rate ($Cv^{-1/2}$). Linear fitting is used to calculate the standard HET rate constant (k^0). All measurements were performed relative to external Ag/AgCl (3 M KCl) reference electrode.

four LSG and Pt/LSG are shown in Figures S7 and S8 in the Supporting Information), which are presented in **Table 1**. The relative standard deviation for each parameter has been calculated and it suggests repeatability. From the slope, the average k^0 value is calculated to be 0.1150 cm s^{-1} for $[Fe(CN)_6]^{4-}$, which is better than other types of sp^2 carbon surfaces such as graphene on copper electrode ($\approx$0.014 cm s^{-1}), laser induced graphene from GO (0.02373 cm s^{-1}) and Q-graphene (0.0186 cm s^{-1}), demonstrating a favorable electron transfer rate in the case of 3D porous LSG (**Table 2**).[7d,20] Recent literature on graphene based electrodes has also proven to have favorable electron

transfer kinetics compared to graphite based electrodes [EPPG (0.022 cm s^{-1}) and BPPG (10^{-9} cm s^{-1})].[21] Pumera and co-workers reported electron transfer is about 35 times faster in stacked graphene platelet nanofibers (SGNFs) with open edges than with folded edges.[22] Being the edge plane electron transfer kinetics are anomalously faster than that of inert basal plane; the enhancement is believed to be a combined consequence of the porous, binder free 3D network of LSG with large intrinsic protrusions of graphene sheets and rich in edge plane sites which, in turn, activate the graphene surface toward enhanced electrochemical reactions. Further, the calculated k^0

Table 1. Stochastic electrochemical performance metrics of LSG and Pt/LSG electrodes.

Electrodes	Electrochemical active surface area A [mm^2]		[Fe(CN)$_6$]$^{4-}$				[Ru(NH$_3$)$_6$]$^{3+}$			
			LSG		Pt/LSG		LSG		Pt/LSG	
	LSG	Pt/LSG	ΔE_p [mV]	k^0 [cm s^{-1}]	ΔE_p [mV]	k^0 [cm s^{-1}]	ΔE_p [mV]	k^0 [cm s^{-1}]	ΔE_p [mV]	k^0 [cm s^{-1}]
1	9.370	10.365	84	0.11869	69	0.32008	94	0.09055	74	0.2418
2	9.023	10.760	87	0.10842	71	0.26847	97	0.08286	75	0.22112
3	9.158	10.331	82	0.13439	68	0.35965	94	0.08776	75	0.22251
4	9.241	10.174	87	0.10877	74	0.25055	96	0.09183	74	0.23148
5	9.095	10.285	88	0.10460	72	0.21259	94	0.08081	74	0.23907
Average	9.177	10.383	85.6	**0.1150**	70.8	**0.2823**	95	**0.0868**	74.5	**0.2312**
RSD (%)	1.46	2.14	2.93	4.98	3.37	20.55	2.93	5.52	0.74	4.05

www.MaterialsViews.com

**ADVANCED
ELECTRONIC
MATERIALS**

www.advelectronicmat.de

FULL PAPER

Table 2. HET rate (k^0) of two redox mediators on LSG and Pt/LSG compared with similar carbon based electrode materials. Pt nanoparticles decorated laser scribed graphene (Pt/LSG); laser scribed graphene (LSG); basal plane pyrolytic graphite (BPPG); edge plane pyrolytic graphite (EPPG); laser induced graphene from GO (L-graphene); graphene grown on copper foil by chemical vapor deposition (CVD-Gr); polyhedral structure graphene (Q-graphene); few-layer (termed quasi-) graphene grown via CVD (q-graphene); mono-layer graphene grown via CVD (m-graphene).

Electrodes	k^0 [cm s^{-1}]		References
	[Fe(CN)6]4–	[Ru(NH3)6]3+	
Pt/LSG	**0.2823**	**0.2312**	**Present work**
LSG	**0.1150**	**0.0868**	**Present work**
BPPG	10^{-9}	0.0038	[21,23]
EPPG	0.022	0.00877	[21,23]
L-graphene	0.02373	–	[7d]
CVD-Gr	0.014	0.012	[20a]
Q-graphene	0.0186	0.0177	[20b]
q-graphene	–	0.00158	[23]
m-graphene	–	0.0011	[23]

value for Pt/LSG is 0.2823 cm s^{-1} which elucidates the catalytic behavior of Pt NPs on the surfaces of the LSG facilitating the electron transfer mechanism.

The average k^0 value for [Ru(NH$_3$)$_6$]$^{3+}$ redox mediator on LSG and Pt/LSG electrodes are calculated to be 0.0868 and 0.2312 cm s^{-1}, respectively which is greater than the k^0 measured at the graphene on copper electrode ($\approx$0.012 cm s^{-1}),[20a] Q-graphene (0.0177 cm s^{-1}),[20b] monolayer-graphene (0.0011 cm s^{-1}), quasi-graphene (0.00158 cm s^{-1}), BPPG (0.0038) and EPPG (0.00877) electrodes, respectively utilizing the ruthenium redox mediator.[23] This is again an evidence of the effective electron transfer kinetics of LSG electrode. The ruthenium complex is interesting because it is an outer-sphere redox mediator solely dependent on the DOS of the electrode material and less sensitive to oxygen content/surface microstructure. In this present scenario, most importantly, LSG electrode exhibits electrochemical kinetics that is several orders of magnitude faster than that of other carbon based electrode materials. The sole reason can be the increased DOS at the edges of graphene (in comparison to basal plane) resulting a faster electrode kinetics.[24] Therefore the difference in DOS between edges and basal plane is favorable for LSG being a 3D porous network of graphene rich in edge sites, which contributes more significantly to its faster electron transfer kinetics. Again, the improved k^0 value indicates that Pt/LSG is more catalytic compared to LSG and can be beneficially utilised in electrochemical sensing applications.

2.3. Biosensor Performance

The electro-oxidation of biologically important molecules and hence its detection on graphene based electrodes mainly relies on the catalytic activity of electrode material and the electron transfer properties. In order to evaluate the sensing ability of LSG electrodes, we studied its inherent electrochemistry toward AA, DA, and UA. DA is one of the important neurotransmitter

in the mammalian central nervous system. Any abnormality leads to severe neurological disorders such as Parkinson's disease and Schizophrenia, and hence is a key marker for the treatment of these diseases. AA is well-known for its antioxidant properties and plays a key role in biological metabolism. UA is an important natural antioxidant produces when body breaks down purines. Abnormal levels of UA are symptomatic of hyperuricemia and several kidney diseases. Because AA, DA, and UA coexist in central nervous system and the electrochemical oxidation peak potentials overlap at conventional solid electrodes, the primary challenge encountered here is to separate their oxidation peak potentials with enhanced intensity.[25]

The sensing ability of LSG based electrodes has been analyzed for the detection of AA, DA, and UA electrochemically using CV and differential pulse voltammetry (DPV). **Figure 6**a–c shows CVs for LSG and Pt/LSG electrode for 1×10^{-3} M DA, UA, and AA in phosphate buffer solution (PBS) as supporting electrolyte. The CVs depict well-defined oxidation current at low potential, which outperforms similar graphene based electrode materials.[26] Again for Pt/LSG, the oxidation current was enhanced compared to that of the LSG electrode. To know the exact oxidation peak separation among the three biomarkers, the electrochemical behavior of the LSG electrode was further studied in PBS containing a mixture of the three analytes (1×10^{-3} M AA, 40×10^{-6} M DA and UA) shown in Figure 6d, which results in voltammetric peak separations of $\Delta E_{AA-DA} = 234$ mV, $\Delta E_{DA-UA} = 134$, and $\Delta E_{AA-UA} = 368$ mV, respectively. These results are better than the reported literature values for graphene based electrode.[27] This can be attributed to the combined advantage from: (i) rapid electron transport properties of porous graphene network, (ii) rich in edge plane like structures enhancing catalytic activity, and (iii) the 3D hierarchical and porous network providing enough accessibility to biomolecules. Again for Pt/LSG results voltammetric peak separations of $\Delta E_{AA-DA} = 236$ mV, $\Delta E_{DA-UA} = 143$ mV, and $\Delta E_{AA-UA} = 379$ mV, respectively, which can be due to the catalytic activity of Pt NPs.

The typical DPV response of the LSG electrode to the addition of different concentrations of DA, UA, and AA in PBS solution is shown in **Figure 7**a–c. The oxidation current is seen increasing linearly as the concentration is increased from 10 to 680×10^{-6} M for AA, 0.5–32.5×10^{-6} M for DA, and 0.5–19.5×10^{-6} M for UA, respectively. Since UA, DA, and AA coexist in biological fluid, the accurate measurements of each component with a high degree of selectivity are highly enviable. We studied the performance of Pt/LSG electrode at various concentrations for each species with the other two species held at fixed concentrations. Figure 7d–f represents the DPV after repeatedly adding different concentrations of AA, UA, and DA while keeping the other two fixed. The current is seen increasing linearly as the concentration is increased from 10 to 890×10^{-6} M for AA, 0.5 to 56×10^{-6} M for DA, and 1 to 63×10^{-6} M for UA for Pt/LSG electrode. It is noticed that the oxidation peak currents remain almost constant for two of the molecules at the expense of selective increase in the current when the concentration of the third one was increased, indicating no significant influence or interference of one species on other two. Very similar trends were observed for the detection of DA and UA, which is a signature of anti-interference ability
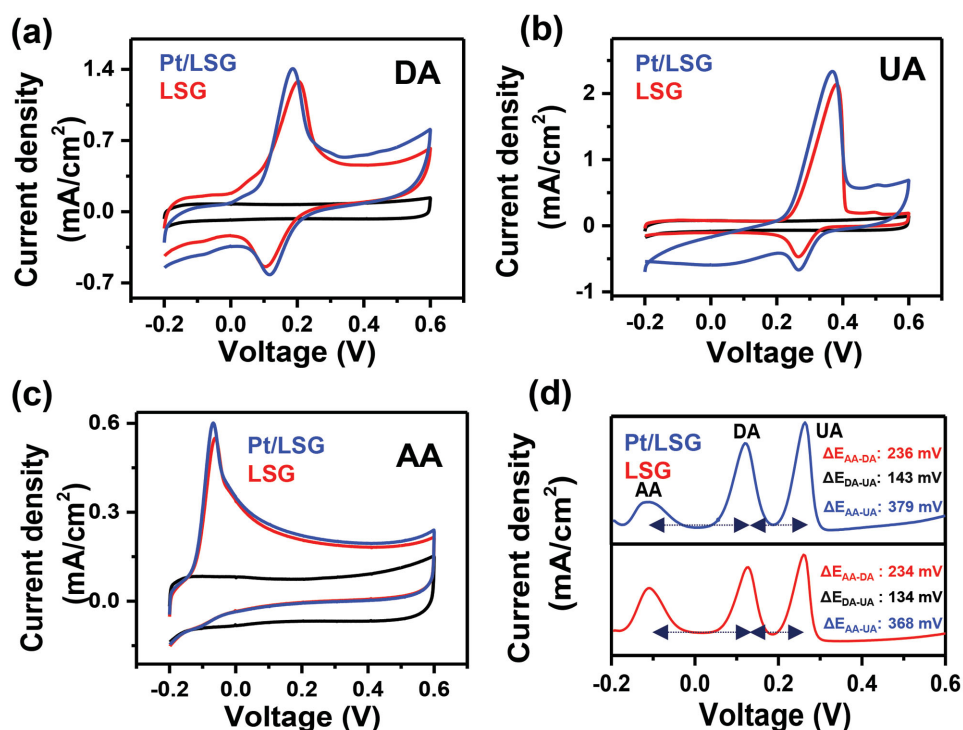
Figure 6. Cyclic voltammograms of LSG and Pt/LSG electrodes in 0.1 M PBS (pH 7.0) containing a) 1×10^{-3} M ascorbic acid (AA), b) 1×10^{-3} M dopamine (DA), and c) 1×10^{-3} M uric acid (UA) at a scan rate of 50 mV s^{-1} compared to response for only buffer solution (black line). d) Differential pulse voltammetry curve of a LSG and Pt/LSG electrodes in 0.1 M PBS (pH 7.0) containing 1×10^{-3} M AA + 40×10^{-6} M DA + 40×10^{-6} M UA. All measurements were performed relative to external Ag/AgCl (3 M KCl) reference electrode.
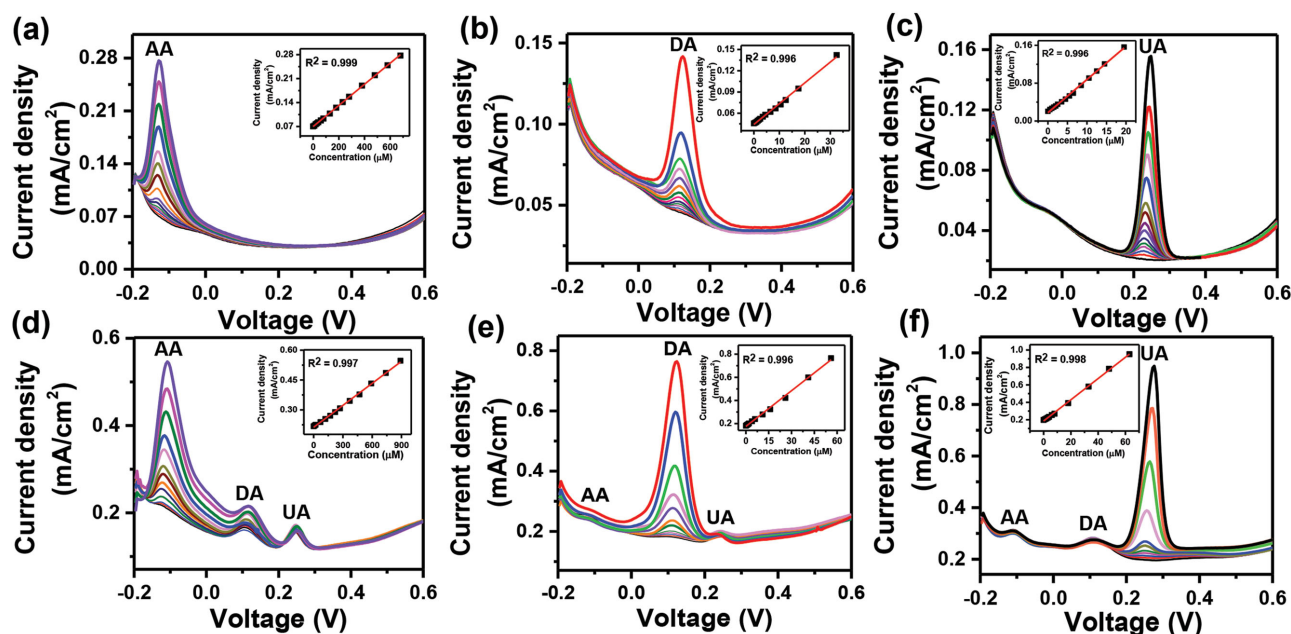

Figure 7. Electrochemical detection of AA, DA, and UA. Differential pulse voltammetry (DPV) at LSG at different concentrations of a) AA, b) DA, and c) UA in 0.1 M PBS (pH 7.0) as supporting electrolyte. DPV at Pt/LSG for various concentrations of d) AA in a mixture of 4×10^{-6} M DA and 4×10^{-6} M UA, e) DA in a mixture of 30×10^{-6} M AA and 4×10^{-6} M UA, f) UA in a mixture of 40×10^{-6} M AA and 4×10^{-6} M DA, Insets: plots of the oxidation peak current density versus concentration of each biomarker. Linear fitting is used to determine the sensitivity of the electrodes for each biomarker. DPV conditions: pulse height = 50 mV, pulse width = 0.2 s, step height = 4 mV, step time = 0.5 s, and scan rate = 8 mV s^{-1}. All measurements were performed relative to external Ag/AgCl (3 M KCl) reference electrode.

of LSG based electrode. The limit of detection (LOD) were calculated based on standard deviation of the response (SD) and the slope (S) of the fitted calibration plots [LOD = 3 × (SD/S)], which were found to be 6.1, 0.07, and 0.22×10^{-6} M for AA, DA, and UA, respectively for Pt/LSG. The sensitivity parameters were calculated from the slope of calibration plot to be 250.69, 6995.6, and 8289 µA mM^{-1} cm^{-2} for AA, DA, and UA, respectively, which are better than those of other nanocarbon-based electrodes in the literature.[26b,28] Compared to DA and UA, a low sensitivity and poor LOD is observed for AA, which can be ascribed due to its weak adsorption strength on electrode surface.[25] All of the analytical parameters obtained from Figure 7 are summarized and compared with the data from the literature (see Table S3 in the Supporting Information). Thus, LSG based electrode may be a promising candidate for biosensing due to their improved selectivity and sensitivity.

2.4. Flexibility Test

The flexibility of the LSG electrode was examined using CV test to probe the effect of bending stress on potential changes on the electrochemical reactivity of the sensors. The electrochemical behavior of the flexible device was thus evaluated under flat, convex and concave bending stresses to imitate diverse deformations in practical applications (**Figure 8**a–f). A solution containing [Fe(CN)$_6$]$^{4-}$ redox mediator at a concentration of 5×10^{-3} M dissolved in 0.1 M KCl as supporting electrolyte was used and a series of CVs were recorded as shown
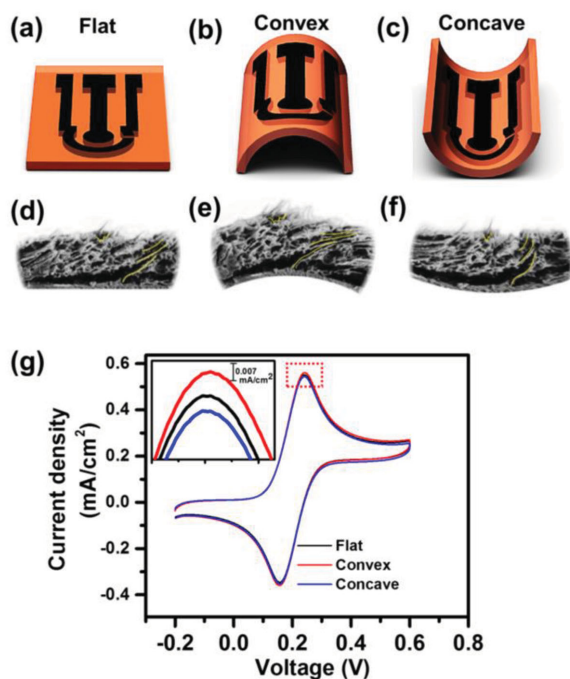
Figure 8. a–c) Schematic illustrations of the LSG electrode and d–f) its simulated cross sectional FE-SEM images in flat, convex, and concave bending stress modes, respectively. g) Corresponding CVs for 5×10^{-3} M [Fe(CN)$_6$]$^{4-}$ at 10 mV s^{-1} scan rate. The measurements were performed relative to external Ag/AgCl (3 M KCl) reference electrode and 0.1 M KCl solution was used as supporting electrolyte.

in Figure 8g. Upon several times convex and concave bending, there appeared negligible change in the J_p ($\Delta J_{\text{p-convex}}$ = 0.64% and $\Delta J_{\text{p-concave}}$ = 0.43%) suggesting the mechanical stability of device.

3. Conclusions

Large scale flexible electrochemical sensors were fabricated by direct growth of graphitic carbon patterns on a commercial polyimide surface employing a laser scribing approach. The key characteristics of the laser scribed graphene include self-standing macro/mesoporos 3D morphology with ample amount of edge plane sites and large electrochemical surface area. Co-planar electrode architecture along with the binder-free porous network, facilitates ion diffusion leading to efficient electron transfer. The heterogeneous electron transfer kinetics using both inner-sphere [Fe(CN)$_6$]$^{4-}$ and outer-sphere [Ru(NH$_3$)$_6$]$^{3+}$ redox mediators revealed quasi-reversible electron transfer at the LSG electrode surface, with electron transfer rate (k^0) of 0.1150 and 0.0868 cm s^{-1}, respectively. Further, the electron transfer kinetics were improved by selective anchoring of Pt NPs on the laser scribed electrodes. The LSG electrode patterns exhibited significantly improved electrocatalytic performance toward oxidation of ascorbic acid, dopamine and uric acid as displayed by an enlarged peak separation of $\Delta E_{\text{AA–DA}}$ = 234 and 236 mV, $\Delta E_{\text{DA–UA}}$ = 134 and 143 mV and $\Delta E_{\text{AA–UA}}$ = 368 and 379 mV for LSG and Pt/LSG, respectively. Simultaneous detection of these biomarkers was achieved with high sensitivity and selectivity in a wide concentration range. Our sensor performance shows that laser scribed graphene electrodes are very promising and excellent platform for developing printed electrochemical sensors for a wide range of analytical applications.

4. Experimental Section

Reagents and Materials: Kapton, trade name for PI sheet (125 µm thickness) was purchased from Dasom RMS Co. LTD. Prior to use, the sheet was cleaned by rinsing with ethanol followed by water and then dried off by blowing nitrogen. Potassium ferrocyanide K$_4$[Fe(CN)$_6$], hexaaminruthenium(III) chloride [Ru(NH$_3$)$_6$ Cl$_3$, 98%], potassium chloride (KCl, 99%), dopamine hydrochloride (DA, (HO)$_2$C$_6$H$_3$CH$_2$CH$_2$NH$_2$·HCl), uric acid (UA, C$_5$H$_4$N$_4$O$_3$) (≥99%), and L-ascorbic acid (AA, C$_6$H$_8$O$_6$), perchloric acid (HClO$_4$), chloroplatinic acid (H$_2$PtCl$_6$·6H$_2$O) were purchased from Sigma Aldrich. The reagents were of analytical grade and were used as received. All stock solutions were prepared using deionized (DI) water (18.2 MΩ cm, Milli-Q Direct 8, Merck Millipore, and Billerica, MA) without further purification. PBS was purchased from Fisher Scientific-US. Freshly prepared UA, DA hydrochloride, and AA solutions of required concentrations were used regularly for electrochemical experiments. SYLGARD 184 silicone Elastomer comprising of base elastomer/curing Agent (Dow Corning) were mixed in a 10 (base):1 (curing agent) ratio by weight manually and was degassed by keeping under vacuum for 30 min in order to remove air bubbles prior to use as passivation layer on LSG electrodes. Conducting silver paint was procured from TED Pella, USA.

Device Fabrication: Fabrication of LSG Patterns—Laser scribing was performed on PI sheet by CO$_2$ Universal Laser system (Universal X-660 laser cutter platform, Professional laser system PLS6.75, laser peak power 75 W): 10.6 µm wavelength of laser with pulse duration of ≈14 µs. The laser system was equipped with X–Y control stage with

varying scan rates from 0.7 to 23 in. s^{-1}. Typical values of power could be varied from 2.4 to 5.4 W with the pulses per inch (PPI) in a range of 1 to 1000. PPI setting allowed in controlling laser pulses per linear inch, the laser cartridge emitted. Hence, PPI setting of 100% corresponded to an absolute value of 1000 pulses per inch. Laser power (peak power, speed, PPI, and the Z-distance between laser and the sample were optimized to 15%, 10%, and 1000 and 2 mm, respectively. Corel draw software was employed to design the three electrode patterns on PI sheet. The beam size was roughly around 100 µm. All of the laser scribing experiments were performed under ambient conditions.

LSG was patterned into three electrode system with a dimension of 2 cm × 1.2 cm. The working electrode was designed with a fixed diameter of 3 mm. A minimum spacing of ≈500 µm was maintained between two neighboring microelectrodes (Figure S1a, Supporting Information). These carbon patterns having a typical thickness ≈33 µm, qualified them to be referred as microelectrodes (as the thickness is of a few tens of micrometers). PDMS was used as passivation layer to define the working electrode area (3 mm diameter) exactly and was cured at 85 °C for 30 min (Figure S1b, Supporting Information). Thereafter, the graphitic electrodes were externally connected with conductive copper tape glued by silver paste to ensure better electrical contact (Figure S1c, Supporting Information).

Synthesis of Pt/LSG Pattern: Electrodeposition of Pt NPs on the LSG WE was done with a three-electrode setup comprising external Pt wire as counter electrode, Ag/AgCl as reference electrode and the WE drawn on PI sheet (with a diameter of 3 mm) as working electrode. The LSG CE and RE were not connected in order to prevent from any kind of electrochemical reaction. The electrodes were immersed into an aqueous solution containing 2×10^{-3} M PtCl$_6^{2-}$ and 0.5 M perchloric acid. Deposition of Pt NPs on LSG was induced by stepping the potential from 0.0 to −0.5 V for 5 s. The loading amount of Pt NPs onto LSG was controlled by adjusting the deposition time and optimized parameters that were used for deposition in all electrodes used for the study. After electrodeposition, the patterned three-electrode on PI sheet was removed from the cell and washed thoroughly with DI water to remove excess or unwanted electrolyte salts devoid of electrode patterns and then placed in a vacuum oven at 60 °C.

Material and Electrochemical Characterizations: XRD patterns were collected by a Bruker diffractometer (D8 Advance) with Cu K$_\alpha$ radiation, λ = 1.5406 Å. The morphology and microstructure of the samples were characterized by high-resolution field emission scanning electron microscopy (Nova Nano 630, FEI) and high-resolution transmission electron microscopy (Titan 80–300 kV). Cross-sectional SEM was employed to measure the thickness of LSG films. TEM samples were prepared by peeling off graphene/Pt-G from a laser scribed PI substrate, followed by sonicating them in alcohol and dropping them onto a carbon copper grid. Raman spectroscopy measurements were carried out on the samples using a micro-Raman spectrometer (LabRAM ARAMIS, Horiba-Jobin Yvon). Raman spectra acquired with notch filters cutting at 100 cm^{-1} using a Cobalt laser (473 nm, 5 mW at source). The contact angle was imaged using Theta/Attension optical tensiometer with DI water droplet.

All the electrochemical measurements were performed using a CHI 608D workstation (Austin, USA). Cyclic voltammetry) and DPV were used as the main techniques to characterize the patterned electrodes and for the detection of biomarkers. All of the measurements were conducted under ambient conditions.

Supporting Information

Supporting Information is available from the Wiley Online Library or from the author.

Acknowledgements

[1] a) D. Chen, L. Tang, J. Li, *Chem. Soc. Rev.* **2010**, *39*, 3157; b) W. Yang, K. R. Ratinac, S. P. Ringer, P. Thordarson, J. J. Gooding, F. Braet, *Angew. Chem. Int. Ed.* **2010**, *49*, 2114.

[2] a) W. Li, C. Tan, M. Lowe, H. Abruna, D. Ralph, *ACS Nano* **2011**, *5*, 2264; b) S. Banerjee, J. Shim, J. Rivera, X. Jin, D. Estrada, V. Solovyeva, X. You, J. Pak, E. Pop, N. Aluru, R. Bashir, *ACS Nano* **2013**, *7*, 834; c) W. Yuan, Y. Zhou, Y. Li, C. Li, H. Peng, J. Zhang, Z. Liu, L. Dai, G. Shi, *Sci. Rep.* **2013**, *3*, 2248.

[3] a) X. Dong, X. Wang, L. Wang, H. Song, H. Zhang, W. Huang, P. Chen, *ACS Appl. Mater. Interfaces* **2012**, *4*, 3129; b) X. Dong, H. Xu, X. Wang, Y. Huang, M. B. C. Park, H. Zhang, L. Wang, W. Huang, P. Chen, *ACS Nano* **2012**, *6*, 3206; c) Y. Ma, M. Zhao, B. Cai, W. Wang, Z. Ye, J. Huang, *Chem. Commun.* **2014**, *50*, 11135; d) S. Mao, K. Yu, J. Chang, D. A. Steeber, L. E. Ocola, J. Chen, *Sci. Rep.* **2013**, *3*, 1696; e) J. N. Tiwari, V. Vij, K. C. Kemp, K. S. Kim, *ACS Nano* **2016**, *10*, 46.

[4] a) N. Li, Q. Zhang, S. Gao, Q. Song, R. Huang, L. Wang, L. Liu, J. Dai, M. Tang, G. Cheng, *Sci. Rep.* **2013**, *3*, 1604; b) Z. S. Wu, Y. Sun, Y. Z. Tan, S. Yang, X. Feng, K. Mullen, *J. Am. Chem. Soc.* **2012**, *134*, 19532; c) M. Wu, S. Meng, Q. Wang, W. Si, W. Huang, X. Dong, *ACS Appl. Mater. Interfaces* **2015**, *7*, 21089; d) H. J. Qiu, Y. Guan, P. Luo, Y. Wang, *Biosens. Bioelectron.* **2015**, 10.1016/j.bios.2015.12.029.

[5] a) E. A. Jakus, E. B. B. Secor, A. L. Rutz, S. Jordan, M. C. Hersam, R. N. Shah, *ACS Nano* **2015**, *9*, 4636; b) Q. Zhang, F. Zhang, S. P. Medarametla, H. Li, C. Zhou, D. Lin, *Small* **2016**, *12*, 1702; c) A. E. Jakus, E. B. Secor, A. L. Rutz, S. Jordan, M. C. Hersam, R. N. Shah, *ACS Nano* **2015**, *9*, 4636.

[6] a) S. Lawes, A. Riese, Q. Sun, N. Cheng, X. Sun, *Carbon* **2015**, *92*, 150; b) H. Korhonen, L. H. Sinh, N. D. Luong, P. Lehtinen, T. Verho, J. Partanen, J. Seppälä, *Phys. Status Solidi A* **2015**, *213*, 982.

[7] a) M. F. El-Kady, V. Strong, S. Dubin, R. B. Kaner, *Science* **2012**, *335*, 1326; b) M. F. El-Kady, R. B. Kaner, *ACS Nano* **2014**, *8*, 8725; c) V. Strong, S. Dubin, M. F. El-Kady, A. Lech, Y. Wang, B. H. Weiller, R. B. Kaner, *ACS Nano* **2012**, *6*, 1395; d) K. Griffiths, C. Dale, J. Hedley, M. D. Kowal, R. B. Kaner, N. Keegan, *Nanoscale* **2014**, *6*, 13613.

[8] a) J. Lin, Z. Peng, Y. Liu, F. Ruiz-Zepeda, R. Ye, E. L. Samuel, M. J. Yacaman, B. I. Yakobson, J. M. Tour, *Nat. Commun.* **2014**, *5*, 5714; b) R. Ye, Z. Peng, T. Wang, Y. Xu, J. Zhang, Y. Li, L. G. Nilewski, J. Lin, J. M. Tour, *ACS Nano* **2015**, *9*, 9244; c) L. Li, J. Zhang, Z. Peng, Y. Li, C. Gao, Y. Ji, R. Ye, N. D. Kim, Q. Zhong, Y. Yang, H. Fei, G. Ruan, J. M. Tour, *Adv. Mater.* **2016**, *28*, 838; d) Z. Peng, J. Lin, R. Ye, E. L. Samuel, J. M. Tour, *ACS Appl. Mater. Interfaces* **2015**, *7*, 3414.

[9] T. M. Day, P. R. Unwin, N. R. Wilson, J. V. Macpherson, *J. Am. Chem. Soc.* **2005**, *127*, 10639.

[10] P. Nayak, P. N. Santhosh, S. Ramaprabhu, *J. Phys. Chem. C* **2014**, *118*, 5172.

[11] A. C. Ferrari, J. C. Meyer, V. Scardaci, C. Casiraghi, M. Lazzeri, F. Mauri, S. Piscanec, D. Jiang, K. S. Novoselov, S. Roth, A. K. Geim, *Phys. Rev. Lett.* **2006**, *97*, 187401.

[12] K. S. Subrahmanyam, A. K. Manna, S. K. Pati, C. N. R. Rao, *Chem. Phys. Lett.* **2010**, *497*, 70.

[13] M. Pumera, *Electrochem. Commun.* **2013**, *36*, 14.

Materials
Views
www.MaterialsViews.com

ADVANCED
ELECTRONIC
MATERIALS
www.advelectronicmat.de

FULL PAPER

[14] D. A. C. Brownson, D. K. Kampouris, C. E. Banks, *Chem. Soc. Rev.* **2012**, *41*, 6944.

[15] A. J. Bird, L. R. Faulkner, *Electrochemical Methods*, 2nd ed., John Wiley & Sons, New York **2010**.

[16] a) P. Nayak, B. Anbarasan, S. Ramaprabhu, *J. Phys. Chem. C* **2013**, *117*, 13202; b) Y. Wang, J. G. Limon-Petersen, R. G. Compton, *J. Electroanal. Chem.* **2011**, *652*, 13.

[17] A. N. Patel, M. G. Collignon, M. A. O'Connell, W. O. Hung, K. McKelvey, J. V. Macpherson, P. R. Unwin, *J. Am. Chem. Soc.* **2012**, *134*, 20117.

[18] X. Ji, C. E. Banks, A. Crossley, R. G. Compton, *Chem. Phys. Chem.* **2006**, *7*, 1337.

[19] R. S. Nicholson, *Anal. Chem.* **1965**, *37*, 1351.

[20] a) C. B. Navarro, Z. P. Laker, J. P. Rourke, N. R. Wilson, *Phys. Chem. Chem. Phys.* **2015**, *17*, 29628; b) E. P. Randviir, D. A. Brownson, M. Gomez-Mingot, D. K. Kampouris, J. Iniesta, C. E. Banks, *Nanoscale* **2012**, *4*, 6470.

[21] T. J. Davies, R. R. Moore, C. E. Banks, R. G. Compton, *J. Electroanal. Chem.* **2004**, *574*, 123.

[22] A. Ambrosi, A. Bonanni, M. Pumera, *Nanoscale* **2011**, *3*, 2256.

[23] D. A. Brownson, S. A. Varey, F. Hussain, S. J. Haigh, C. E. Banks, *Nanoscale* **2014**, *6*, 1607.

[24] D. A. C. Brownson, L. J. Munro, D. K. Kampouris, C. E. Banks, *RSC Adv.* **2011**, *1*, 978.

[25] H. Y. Yue, S. Huang, J. Chang, C. Heo, F. Yao, S. Adhikari, F. Gunes, L. C. Liu, T. H. Lee, E. S. Oh, B. Li, J. J. Zhang, T. Q. Huy, N. V. Luan, Y. H. Lee, *ACS Nano* **2014**, *8*, 1639.

[26] a) J.-L. Chang, K.-H. Chang, C.-C. Hu, W.-L. Cheng, J.-M. Zen, *Electrochem. Commun.* **2010**, *12*, 596; b) C. L. Sun, H. H. Lee, J. M. Yang, C. C. Wu, *Biosens. Bioelectron.* **2011**, *26*, 3450.

[27] a) S.-M. Li, S.-Y. Yang, Y.-S. Wang, C.-H. Lien, H.-W. Tien, S.-T. Hsiao, W.-H. Liao, H.-P. Tsai, C.-L. Chang, C.-C. M. Ma, C.-C. Hu, *Carbon* **2013**, *59*, 418; b) C.-L. Sun, C.-T. Chang, H.-H. Lee, J. Zhou, J. Wang, T.-K. Sham, W.-F. Pong, *ACS Nano* **2011**, *5*, 7788.

[28] a) W. Gao, X. Feng, T. Zhang, H. Huang, J. Li, W. Song, *ACS Appl. Mater. Interfaces* **2014**, *6*, 19109; b) Z. Dursun, B. Gelmez, *Electroanalysis* **2010**, *22*, 1106; c) P. Gai, H. Zhang, Y. Zhang, W. Liu, G. Zhu, X. Zhang, J. Chen, *J. Mater. Chem. B* **2013**, *1*, 2742; d) C. Xiao, X. Chu, Y. Yang, X. Li, X. Zhang, J. Chen, *Biosens. Bioelectron.* **2011**, *26*, 2934; e) X. Dong, Y. Ma, G. Zhu, Y. Huang, J. Wang, M. B. Chan-Park, L. Wang, W. Huang, P. Chen, *J. Mater. Chem.* **2012**, *22*, 17044; f) J. Liu, Z. He, J. Xue, T. T. Yang Tan, *J. Mater. Chem. B* **2014**, *2*, 2478.